

New Constraints on the Jovian Narrowband Radio Components from Juno/Waves Observations and 3D Geometrical Simulations

A. Boudouma^{1,2}, P. Zarka², C.K. Louis², M. Imai¹, C. Briand²

¹Department of Space Physics, Institute of Atmospheric Physics, Czech Academy of Science, Prague, Czechia

²LIRA, Observatoire de Paris, CNRS, PSL, Sorbonne Université, Université Paris Cité, Meudon, France

Key Points:

- We applied the 3D geometrical model LsPRESSO to study the generation mechanisms of the jovian narrowband components.
- nKOM is more consistent with ω_{pe} and/or $2\omega_{pe}$ in X-mode at low-latitude, and ω_{pe} in O-mode at high-latitude.
- nLF is consistent with ω_{pe} and $2\omega_{pe}$ in O-mode at all latitudes, but also at $2\omega_{pe}$ in X-mode at low-latitudes.

arXiv:2603.19346v1 [physics.space-ph] 19 Mar 2026

Corresponding author: Adam Boudouma, boudouma@ufa.cas.cz

Abstract

Measurements of Waves instrument onboard the Juno spacecraft suggest that narrowband kilometric radiation (nKOM; 20–141 kHz) and narrowband low-frequency radiation (nLF; 5–70 kHz) are generated within the plasma near the Io plasma torus (IPT) in low-latitude regions. While these emissions are thought to result from the conversion of the natural modes of the plasma into escaping radio waves, at either the fundamental or the first harmonic of the plasma frequency, there is no consensus on the specific mechanism involved. Using the electron density and the magnetic field data from the Jovian Auroral Distribution Experiment (JADE) and the FluxGate Magnetometer (FGM), we determine the range of frequencies accessible to different wave modes during Juno’s crossing of the plasma disk environment. We classify the observed nKOM and nLF according to their propagation modes: trapped (Z-mode or Whistler), escaping (X-mode or O-mode), and undetermined (either trapped or escaping). We apply the 3D numerical modeling method that was developed in Boudouma et al. (2024) to the escaping and undetermined nKOM and nLF observations, deriving macroscopic constraints on the generation mechanisms, wave modes, characteristic frequencies, beaming and source locations. Our results support the interpretation in which high-latitude nKOM is consistent with O-mode, while low-latitude is rather X-mode. Both nKOM and nLF appear to be generated near the fundamental of the plasma frequency, but only nLF shows compatibility with emission near the first harmonic, suggesting the possible coexistence of both linear and nonlinear generation mechanisms.

Plain Language Summary

The Jupiter narrowband kilometric radiation (nKOM) and narrowband low-frequency radiation (nLF), observed by Waves instrument onboard the Juno spacecraft, are believed to be generated in the plasma disk near a region called the Io plasma torus. These radio signals are thought to be generated from the conversion of the plasma energy into electromagnetic waves that can propagate into the vacuum, but the exact process behind this transformation remains uncertain. To better understand how these emissions form, we used measurements of the local plasma and magnetic environment taken by Juno’s JADE and FGM instruments. This helped us identify which types of radio waves could exist in the observed conditions. We then applied a 3D numerical model to analyze the nKOM and nLF emissions. Our findings suggest that nKOM waves seen at high-latitudes match a type called O-mode, while those observed from low-latitudes are more likely X-mode. Both emissions seem to be generated near a key plasma frequency, but only nLF also fits with emission at double that frequency. This points to the possibility of different generation processes occurring together.

1 Introduction

Non-thermal jovian narrowband radiations below 10 MHz were discovered by Voyager Planetary Radio Astronomy (PRA) and Plasma Wave System (PWS) experiments (Warwick et al., 1977, 1979b, 1979a; Kaiser & Desch, 1980; Gurnett et al., 1983; Daigne & Leblanc, 1986). They mostly appear as narrowband kilometric radiation (nKOM) in the range 60–200 kHz (Warwick et al., 1979a; Daigne & Leblanc, 1986; Stone et al., 1992; Reiner et al., 1993; Louarn et al., 1998, 2000, 2001; Zarka et al., 2004; Imai et al., 2017; Louis et al., 2021b). nKOM polarization is predominantly left-handed ordinary mode (O-mode) (Daigne & Leblanc, 1986; Carr et al., 1983; Stone et al., 1992), although occurrences in right-handed extraordinary mode (X-mode) have also been reported (Reiner et al., 1993). The sources of nKOM are distributed at low centrifugal latitudes within the plasma environment nearby the Io Plasma Torus (IPT) (Reiner et al., 1993; Imai et al., 2017) and their modulation periods are between 3% and 5% longer than Jupiter’s rotation period, indicating sub-corotation of the radio sources within the IPT (Kaiser

& Desch, 1980; Stone et al., 1992; Reiner et al., 1993; Louarn et al., 1998, 2000, 2001). Their activation is consistent with intermittent magnetospheric perturbations that induce centrifugal plasma ejection of plasma in the plasma disk (Louarn et al., 1998, 2000, 2001, 2014).

Narrowband low-frequency radiation (nLF), also referred to as escaping continuum radiation (ECR) or very low-frequency radiation (VLF), has been observed in the 5–60 kHz range (Gurnett et al., 1983; Stone et al., 1992; Kaiser et al., 1992; Imai et al., 2017; Louis et al., 2021b; Menietti et al., 2023). Prior to the Juno mission, only a few nLF events had been observed (Gurnett et al., 1983; Stone et al., 1992; Kaiser et al., 1992), as its occurrence probability is relatively low at low-latitudes compared to nKOM (Louis et al., 2021b). Consequently, nLF polarization remains unknown as Juno/Waves does not provide polarization measurements. The source locations of nLF are yet to be confirmed, but limited direction finding measurements suggest that they are distributed at 5° – 10° above the centrifugal equator near the outer edge of the plasma disk (Imai et al., 2017).

Both nKOM and nLF are “plasma emissions” and their generation is attributed to the conversion of the natural modes of the plasma (i.e, electrostatic or trapped electromagnetic waves excited by plasma instabilities) into escaping radio waves at the fundamental or harmonic of the plasma frequency (Jones, 1987; Fung & Papadopoulos, 1987; Reiner et al., 1993; Imai et al., 2017). However, no consensus exists on the nature of the involved mode conversion mechanisms (e.g., linear conversion, waves coupling, wave decay) or on the properties of the resulting radio waves (e.g., frequency, beaming, polarization).

In Boudouma et al. (2024), hereafter referred to as B24, we proposed a numerical method to constrain plasma emissions characteristics based on their large-scale latitudinal beaming. To do so, we developed a 3D geometrical model of the “Large-scale Plasma Radio Emissions Simulation of Spacecraft Observation” (LsPRESSO). We used LsPRESSO to constrain the characteristic frequency, large-scale beaming and cutoff of nKOM based on the Juno/Waves observations (Louis et al., 2021b). We showed that the distribution of nKOM occurrence probability versus latitude and frequency is only consistent with radio waves near the fundamental of the local plasma frequency, with its beaming directed anti-parallel to the local density gradient. Furthermore, we suggested that nKOM observed by Juno/Waves corresponds to O-mode at high-latitude and X-mode at low-latitude.

Here, we propose to extend this study to the characterization of the nLF. Additionally, we use measurements from the Juno Jovian Aurora Distribution Experiment (JADE) (McComas et al., 2017) and the Flux Gate Magnetometer (FGM) (Connerney et al., 2017) to investigate the characteristics of the medium when Juno is crossing the plasma environment near the IPT and derive further observational constraints on the propagation modes of nKOM and nLF, before comparing their distributions with LsPRESSO results.

Section 2 presents the key aspects of the mode conversion mechanisms involved in the generation of radio waves within the plasma disk. Section 3 describes the Juno/Waves, JADE and FGM data used in this study and the observed distributions that we aim to reproduce in our modeling. Section 4 reviews the B24 method and presents the results from the LsPRESSO modeling. Section 5 compares the results obtained with the Juno/Waves observations on the first perijove. Section 6 summarizes the results obtained and discusses the relevance of the potential mode conversion mechanisms in the generation of nKOM and nLF.

2 Generation of X- and O-modes in Io's Plasma Torus

Voyager, Ulysses and Juno observations suggest that the generation of nKOM and nLF takes place near the IPT. The electron plasma frequency ω_{pe} and the electron cyclotron frequency ω_{ce} are:

$$\omega_{pe} = \sqrt{\frac{n_e e^2}{m_e \epsilon_0}} \quad (1)$$

$$\omega_{ce} = \frac{eB}{m_e} \quad (2)$$

where n_e , e and m_e are the electron density, charge and mass, and ϵ_0 is the vacuum permittivity and B is the magnetic amplitude. In the IPT $\omega_{pe} \geq \omega_{ce}$ or $\omega_{pe} \sim \omega_{ce}$, favoring mode conversion mechanisms over the electron cyclotron maser instability (Perraut et al., 1998; Treumann, 2006). Several mode conversion mechanisms, both linear and nonlinear, are presently debated to explain the generation of escaping radio waves (X- and O-modes) in the IPT.

Linear mode conversion (LMC) mechanisms involve the linear transfer of energy from one mode to another. They can explain the generation of escaping radio waves at the fundamental of ω_{pe} . Considering the Jovian case, Jones (1987) proposed the linear conversion of Z-mode into O-mode near ω_{pe} to explain the generation of planetary radio emissions including the nKOM. By assuming a cold collisionless magnetized plasma with weak ∇n_e near the conversion region, he predicts the generation of O-mode for $\nabla n_e \perp \mathbf{B}$. The rays are beamed in two opposite directions making angles β and $\pi - \beta$ with respect to \mathbf{B} in the plane defined by $(\nabla n_e, \mathbf{B})$, with $\beta = \arctan(\sqrt{\omega_{pe}/\omega_{ce}})$. Thus, the radio sources are expected to lie near the equatorial plane where the condition $\nabla n_e \perp \mathbf{B}$ is more likely to be fulfilled. However, the Jones LMC theory has been challenged as its conversion efficiency and beaming are incompatible with the observations of the terrestrial continuum radiation (TCR) (Melrose, 1981; Barbosa, 1982; Ronnmark, 1989; Boardson et al., 2023). Furthermore, the modeling presented in B24 also suggests that this theory is incompatible with the Juno/Waves nKOM observations. Nevertheless, LMC mechanisms present higher conversion efficiencies when considering the plasma inhomogeneous in the conversion region (Ashour-Abdalla & Okuda, 1984; Budden & Jones, 1987). Numerical studies have explored the linear conversion of Langmuir waves into escaping electromagnetic waves at ω_{pe} in a warm collisionless inhomogeneous magnetized plasma (Cairns & Willes, 2005; Kim et al., 2007, 2008, 2013; Schleyer et al., 2013; Schleyer et al., 2014). They have shown that the conversion is more efficient for plasmas with high electron temperatures T_e and for specific angles between ∇n_e and \mathbf{B} , depending on generated modes and density variation length scale (Schleyer et al., 2013; Schleyer et al., 2014). They predict the generation of both X- and O-modes in weakly magnetized plasma, and the generation of O-mode only in magnetized plasmas (Kim et al., 2007, 2008, 2013).

Nonlinear mode conversion (NLMC) mechanisms involve the nonlinear coupling between multiple modes. They can explain the generation of escaping radio waves at both the fundamental and the harmonics of ω_{pe} . Considering the Jovian case, Fung and Papadopoulos (1987) proposed the nonlinear coupling between two Langmuir waves initially at the upper-hybrid frequency $\omega_{uh} = \sqrt{\omega_{pe}^2 + \omega_{ce}^2}$, into X- and O-modes at $2f_{uh}$ beamed perpendicularly to \mathbf{B} , to explain the generation of nKOM. They assumed a cold collisionless magnetized plasma with weak ∇n_e . This generation scenario has also been explored in B24 and we show that it cannot explain the Juno/Waves nKOM observations. Extensive numerical studies have been performed on the nonlinear coupling between beam-driven Langmuir waves into electromagnetic waves as they are the most favored mechanism to explain the generation of type II and III solar bursts (Thurgood & Tsiklauri,

2015; Henri et al., 2019; Krafft & Savoini, 2021; Bacchini & Philippov, 2024; Krafft & Volokitin, 2024). Unlike its linear counterpart, this conversion process can only occur if the Langmuir wave amplitude reaches a given threshold (Henri et al., 2010; Briand et al., 2014) and relies on very different parameters depending on the properties of the plasma. They have shown that in a homogeneous plasma, the conversion at $2\omega_{pe}$ is more dominant than the conversion at ω_{pe} and its efficiency depends on the ratio between electron and ion temperature T_e/T_i (Henri et al., 2019; Bacchini & Philippov, 2024). Also, in the presence of small-scale density fluctuations, the conversion at ω_{pe} is favored in comparison to $2\omega_{pe}$, since linear conversion occurs simultaneously (Krafft & Savoini, 2021; Krafft & Volokitin, 2024; Krafft et al., 2024).

3 Data

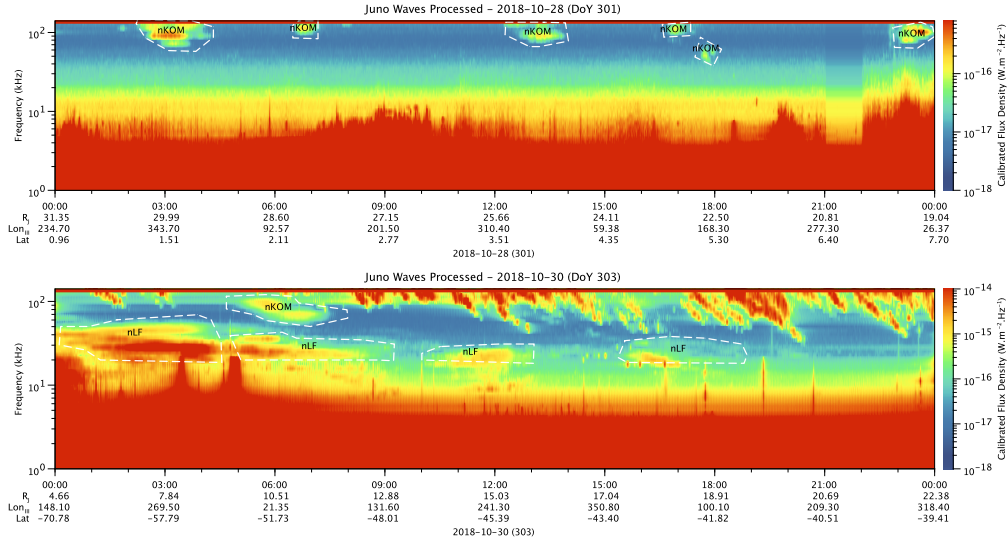


Figure 1. 24-hour dynamic spectra of calibrated Juno/Waves data (Louis et al., 2021b) observed around the 16th perijove PJ16 (top-panel) a day before from low-latitudes (day-of-year 2018-301, i.e., 28/10/2018) and (bottom-panel) a day after from high-latitudes (day-of-year 2018-303, i.e., 30/10/2018). The white boxes correspond to the catalogued nKOM and nLF components with their labels displayed in black (Louis et al., 2021a). The horizontal axis corresponds to the Juno observations time period, radial distance (R_j), system III longitude (Lon_{III}) and jovian latitude (Lat). The vertical axis corresponds to the Juno/Waves frequency channels from 1 kHz to 141 kHz, distributed on a logarithmic scale with a ratio $\times 1.12$ between consecutive channels. The saturated band at 140 kHz correspond to the channel 61 of the HFR-low receiver that has a poor sensitivity.

Figure 1 displays 24-h events of Juno/Waves typical observations one day before and after a perijove (here PJ16). Multiple nKOM and nLF are observed. nKOM is recognizable by its narrowband smooth and fuzzy time-frequency morphology. nLF also displays a similar time-frequency morphology. In comparison to nKOM, nLF patches are observed to be more intense and at lower frequencies. Among the nKOM events visible on Figure 1 top panel, two are observed 10.3 h–10.5 h apart in the range 60 kHz to 140 kHz. Similarly, for the nLF events visible on Figure 1 bottom panel, two are also observed ~ 10 h apart in the range 20 kHz–30 kHz. While the periodicity of the nKOM is caused by the sub co-rotation of the nKOM radio sources in the IPT (Kaiser & Desch, 1980; Reiner

et al., 1993; Louarn et al., 1998, 2000), the cause of the periodicity of the nLF is unknown (Kaiser et al., 1992).

3.1 Latitudinal Beaming of the Jovian Narrowband Radio Components

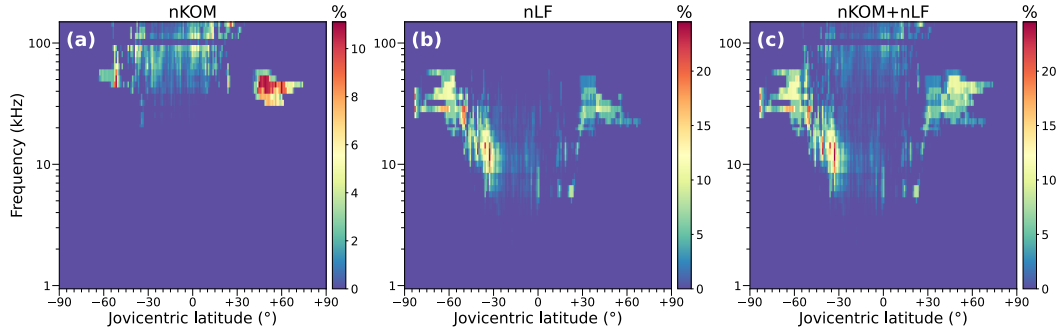


Figure 2. (a) nKOM, (b) nLF and (c) nKOM+nLF occurrence probability versus frequency and latitude derived from the first 3 years of Juno/Waves low-frequency observations around Jupiter by Louis et al. (2021b). The color scale is adjusted in each panel and represents the occurrence probability in %. The latitude correspond to the jovicentric-latitude of observation of the Juno spacecraft and the bins are 1° wide. The frequencies correspond to the Juno/Waves frequency channels from 1 kHz to 141 kHz, distributed on a logarithmic scale with a ratio $\times 1.12$ between consecutive channels. Panels (a) and (b) are based on the same data as Figure S4a and S4b from Louis et al. (2021b), except that no smoothing has been applied.

A catalog of all the jovian radio components observed by Juno/Waves from April 9, 2016 to June 24, 2019 has been compiled based on the emissions time-frequency morphology (Louis et al., 2021a, 2021b). About ~ 2000 nKOM and ~ 1200 nLF events were identified in that time period. Louis et al. (2021b) used the catalog to characterize the latitudinal variation of all the jovian radio components, including the nKOM and the nLF. Figure 2 displays the occurrence probability of (a) nKOM, (b) nLF and (c) nKOM+nLF with respect to the latitude and frequency of observation of Juno/Waves. The nKOM distribution (Figure 2.a) shows a strong North-South asymmetry and is concentrated above 30 kHz, with peaks in the North between $+40^\circ$ and $+75^\circ$ (30–60 kHz), and in the South between -65° and -50° (40–100 kHz). Occurrence minima appear near the equator but are only connected to the Southern peak. The nLF distribution (Figure 2.b) is also asymmetric, mostly below 60 kHz, with a broad Southern peak (-85° to -25°) and a narrower Northern peak ($+25^\circ$ to $+70^\circ$). Equatorial minima are observed between -20° and $+25^\circ$, partially mirroring the pattern seen in nKOM. The combined distribution (Figure 2.c) highlights the complementarity between nKOM and nLF emissions. While peaks in both hemispheres appear connected, equatorial minima remain disconnected, especially between 30 and 40 kHz, forming an arc-like structure in the latitude-frequency space.

The nKOM and nLF radio components share similar time-frequency morphology. Furthermore, the nKOM and nLF radio components seem complementary in the latitude-frequency plane. In addition, Juno/Waves direction findings measurements on two nLF events have found their radio sources to be distributed at the outer edge of the IPT (Imai et al., 2017). Thus, the Juno/Waves observations suggest that the nLF also has its radio sources located near the IPT.

3.2 Propagation Modes

Because of the plasma dispersive-properties, there are radio waves that cannot escape the IPT. The trapped plasma normal-modes are the Whistler mode (W-mode) and the low-frequency branch of the extraordinary mode (Z-mode). The escaping plasma modes are the ordinary mode (O-mode) and the high-frequency branch of the extraordinary mode (X-mode). Because of their resonant properties, the trapped modes are also called the “natural modes” of the plasma and have generation mechanisms that are different from the escaping modes.

We want to characterize the nKOM and nLF depending on their propagation mode. In order to characterize the mode linked to an observed radio wave, the polarization of the measured signal (i.e., the direction of the inbound electric field) and the medium characteristics (i.e., the plasma density and the magnetic field properties) must be determined. However, the Juno/Waves antennas cannot provide data on wave polarization. Nevertheless, Juno’s orbit allows Waves observation inside the IPT ~ 2 days before the perijoves.

Using the Juno JADE estimation of the cold electron density derived from measurement of the electron pitch angle (McComas et al., 2017) and the Juno-MAG magnetic field measurements (Connerney et al., 2017), we are able to estimate locally to Juno the value of ω_{pe} and ω_{ce} . The Juno-JADE and Juno-MAG data are resampled at 1min to match the Juno/Waves calibrated flux density data (Louis et al., 2021b, 2021a). There are gaps in the JADE measurements, resulting in either absence of pitch angle measurements, or because the plasma is too thin in comparison to the JADE instrument sensitivity. In the latter case, we choose to fill the missing data by 0. In the former case, we choose to fill the missing data by linear interpolation.

The JADE ω_{pe} and FGM ω_{ce} estimations are used to identify the frequency range accessible to different wave modes during Juno’s passage through the plasma (see Appendix A). The Juno/Waves nKOM and nLF observations were classified in three groups depending on their observation frequency f with $\omega = 2\pi f$:

1. the trapped emissions: Z- and W-modes (noted ZW-mode), if $f < f_{pe}$
2. the escaped emissions: X- and O-modes (noted XO-mode), if $f > f_{uh}$
3. the undeterminable emissions: Z- and O-modes (noted ZO-mode), if $f_{pe} < f < f_{uh}$

Figure 3 displays the occurrence probability of nKOM, nLF and nKOM+nLF in ZW-, XO- and ZO-modes with respect to the latitude and frequency of the Juno/Waves observations. nKOM appears exclusively in XO- and ZO-modes. XO-mode occurrences (Figure 3.b) are found above 40 kHz between -55° and $+40^\circ$, corresponding to low-latitude emissions. ZO-mode occurrences (Figure 3.c) are seen between 30–60 kHz at high-latitudes ($< -50^\circ$ and $> +40^\circ$), indicating a separation between low- and high-latitude sources. nLF is observed in all three modes. ZW-mode occurrences (Figure 3.d) appear below 30 kHz in the Northern hemisphere ($+10^\circ$ to $+60^\circ$). XO-mode events (Figure 3.e) occur over a broad latitude range (-55° to $+35^\circ$) above 5 kHz. ZO-mode events (Figure 3.f) are concentrated between 20–50 kHz, with a notable low-frequency extension down to 7 kHz in the North. The combined distribution confirms these patterns. ZW-mode (Figure 3.g) is identical to the nLF distribution (Figure 3.d). In XO-mode (Figure 3.h), a gap appears at 30–40 kHz near the equator, separating nKOM and nLF. In ZO-mode (Figure 3.i), the Northern and Southern peaks of both components show continuity across latitude.

As this study focuses on the generation of the nKOM and nLF in the X- and O-modes, we propose to exclude the observations in ZW-mode from the dataset. Nevertheless, only nLF has been observed in ZW-mode. In comparison to the observations in

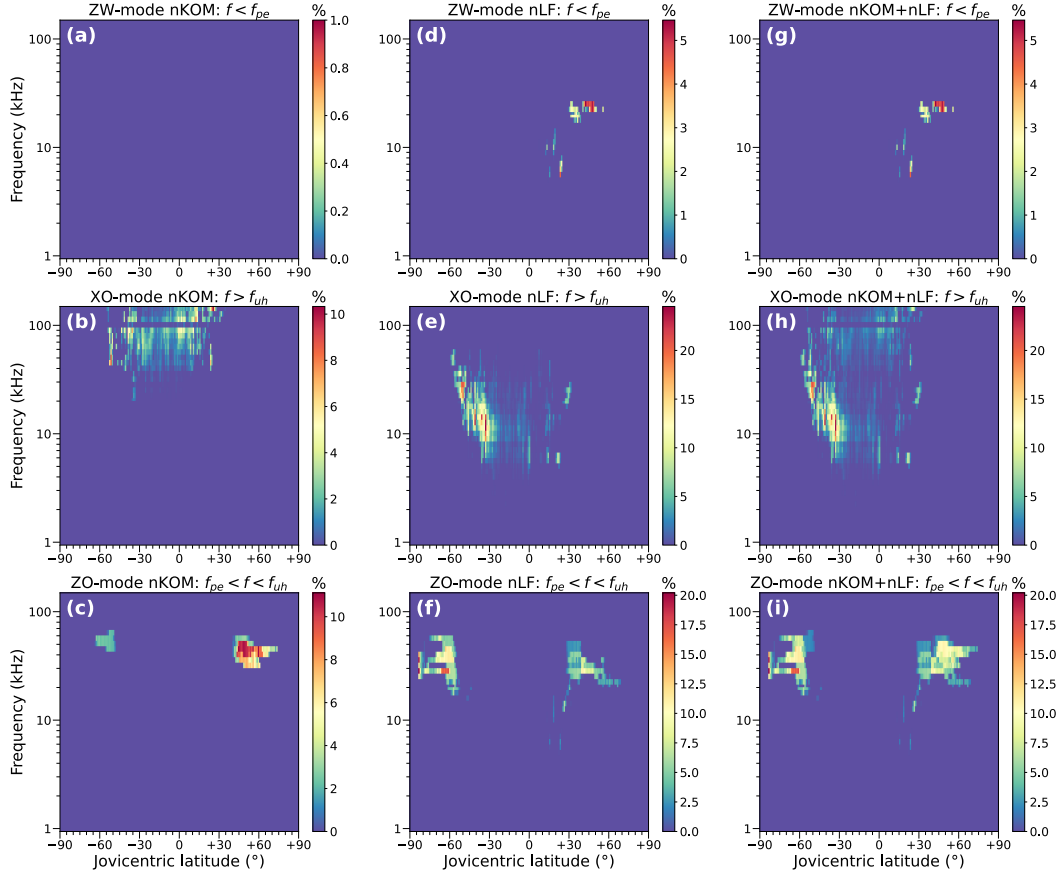


Figure 3. nKOM, nLF and nKOM+nLF occurrence probability versus frequency and latitude in ZW-, XO, and ZO-modes. The color scale is adjusted in each panel and represents the occurrence probability in %. Latitude bins are 1° wide and frequencies correspond to Juno/Waves frequency channels from 10 kHz to 141 kHz, distributed on a logarithmic scale with a ratio $\times 1.12$ between consecutive channels. (a) nKOM in ZW-mode, (b) nKOM in XO-mode, (c) nKOM in ZO-mode, (d) nLF in ZW-mode, (e) nLF in XO-mode, (f) nLF in ZO-mode, (g) nKOM+nLF in ZW-mode, (h) nKOM+nLF in XO-mode and (i) nKOM+nLF in ZO-mode.

XO- and ZO-modes, the observations in ZW-mode represent a very small subset of the total observations: their removal from the dataset does not change the overall structure of the distribution.

4 LsPRESSO: Modeling of the Occurrence Probability Distribution versus the Latitude and Frequency

As discussed in B24, the nKOM and nLF occurrence probability distributions versus latitude and frequency are assumed to be representative of the emissions time-averaged latitudinal beaming at large scale. We also assume that all the potential nKOM and nLF radio sources are permanently active and emitting under the specific conditions described Section 4.1.

We use the Imai (2016) diffusive density model and Connerney et al. (1998) VIP4 magnetic field model to compute the cold electron density n_e and magnetic field vector \mathbf{B} at any point of Jupiter’s inner magnetosphere. The 3D-Cartesian grid used is iden-

tical as in B24, i.e., $-15 \leq x, y \leq +15 R_J$ in the equatorial plane and $-10 \leq z \leq +10 R_J$ along the rotation axis. The grid step is $dl = 0.1 R_J$.

4.1 Large-Scale Generation Scenarios and Parameters

LsPRESSO is used to simulate the Juno/Waves observations of escaping radio waves produced inside the IPT at large-scale. As proposed in B24, two generation scenarios can be constructed based on the theoretical models discussed in Section 2:

- Scenario #1, based on the theory of Jones (1980): Generation of Jovian plasma emissions at the fundamental plasma frequency, $\omega \sim \omega_{pe}$, in the directions $\mathbf{r}+$ and $\mathbf{r}-$, such that $\angle(\mathbf{r}\pm, \mathbf{B}) = \frac{\pi}{2} \mp (\frac{\pi}{2} - \beta)$, with $\beta = \arctan(\sqrt{\omega_{pe}/\omega_{ce}})$.
- Scenario #2, based on the theory of Fung and Papadopoulos (1987): Generation of Jovian plasma emissions at the first harmonic of the upper-hybrid frequency, $\omega \sim 2\omega_{uh}$, in all directions $\mathbf{r} \perp \mathbf{B}$.

The Snell-Descartes law shows that the waves beaming tends to align with the normal to the refractive index iso-surfaces if this index varies quickly. The resulting ray is aligned with $-\nabla n_e$ in O-mode but also in X-mode (if $\omega_{pe} \gg \omega_{ce}$). At large-scale, such beaming occurs for radio waves produced near ω_{pe} as the refractive index varies quickly after the cutoff (cf. Figure A1). This also can be the case for radio waves produced near $2\omega_{pe}$ if ∇n_e is strong. Thus, we propose two additional generation scenarios where the ray direction is $\mathbf{r} \parallel -\nabla n_e$:

- Scenario #3: near the fundamental $f \sim \omega_{pe}$, consistent with linear and nonlinear conversion mode mechanisms.
- Scenario #4: near the first harmonic $f \sim 2\omega_{pe}$, consistent with nonlinear conversion mode mechanisms.

As seen in the Section 2, LMC mechanisms are mainly controlled by the electron temperature and the angle between the density gradient and the magnetic field. In contrast, NLMC mechanisms are primarily constrained by the Langmuir waves amplitude, the temperature ratio between ion and electron species, and small-scale plasma density fluctuations. However, the Imai (2016) diffusive density model does not allow for the calculation of the plasma electron temperature, making it difficult to use for estimating the Langmuir waves amplitude or the density fluctuations order of magnitude.

Thus, we choose to constrain the activation of sources with the same parameters as in B24:

- The angle between the large-scale density gradient and the magnetic field vector, $\angle(\nabla n_e, \mathbf{B})$. This parameter is related to LMC mechanisms and potentially to NLMC mechanisms (as in the theory of Fung and Papadopoulos (1987)).
- The large-scale density gradient magnitude, $\|\nabla n_e\|$. This parameter is associated with both LMC and NLMC mechanisms. Additionally, it accounts for the large-scale plasma dispersive effects and helps to constrain the validity of the assumptions proposed by generation scenarios regarding the beam directivity.

4.2 Results

Table 1 summarizes the generation scenarios proposed for simulating Jovian plasma emissions.

The activation condition of radio sources is constrained by the parameter pair α and ϵ . The parameter α represents the angle $\angle(\nabla n_e, \mathbf{B})$ and varies within the range $\alpha \in [0^\circ, 90^\circ]$ in steps of 3° . The parameter ϵ is defined as the percentile of $\|\nabla n_e\|$ at each

Table 1. Generation scenarios of Jovian plasma emissions simulated with LsPRESSO.

Generation Scenario	Frequency	Directivity
#1: LMC Jones (1980)	ω_{pe}	$\angle(\mathbf{r}\pm, \mathbf{B}) = \frac{\pi}{2} \mp (\frac{\pi}{2} - \beta)$
#2: NLMC Fung & Papadopoulos (1987)	$2\omega_{uh}$	$\angle(\mathbf{r}, \mathbf{B}) = \frac{\pi}{2}$
#3: Fundamental Plasma Frequency	ω_{pe}	$\angle(\mathbf{r}, \nabla n_e) = \pi$
#4: Harmonic Plasma Frequency	$2\omega_{pe}$	$\angle(\mathbf{r}, \nabla n_e) = \pi$

observation frequency, varying within $\epsilon \in [0\%, 100\%]$ in steps of 10%. For each generation scenario and each pair (α, ϵ) , a time-frequency visibility map is modeled by computing the visibility of emissions at all positions and observation frequencies of Juno/Waves. Their compatibility with the nKOM and nLF observations is deduced by comparing the modeled latitude and frequency distribution to the observed ones using the method introduced in B24, i.e. by retrieving the set of parameters (α, ϵ) that maximizes the linear correlation coefficient C between the observed and modeled distributions. The complete step-by-step process is fully detailed in B24 at the end of Section 4.2.

Table 2 summarizes, for each generation scenario, the maximum value of the linear correlation coefficient C_{max} obtained between the modeled distribution and the observed distributions of nKOM, nLF, and nKOM+nLF observed by Juno/Waves, independently of the mode, in XO and in ZO. The Figures summarizing the results obtained for all distributions observed by Juno/Waves are presented in the Supplementary Informations.

Table 2. Maximum value of the linear correlation coefficient C_{max} between the simulated distributions for each generation scenario and the observed distributions of nKOM, nLF, and nKOM+nLF measured by Juno/Waves, without mode distinction (i.e., global distribution), in XO and in ZO. Values of $C_{max} > 35\%$ are highlighted in bold.

Cutoff	Scenario	Correlation Maximum C_{max}								
		nKOM			nLF			nKOM+nLF		
		Global	XO	ZO	Global	XO	ZO	Global	XO	ZO
O-mode	#1	21%	26%	22%	-2%	5%	9%	8%	1%	12%
	#2	23%	51%	0%	1%	2%	-1%	13%	24%	-1%
	#3	39%	27%	37%	41%	48%	22%	44%	46%	29%
	#4	22%	25%	20%	41%	45%	55%	45%	41%	54%
X-mode	#1	11%	20%	0%	-1%	0%	9%	4%	6%	9%
	#2	22%	50%	0%	1%	2%	-1%	12%	21%	-1%
	#3	24%	47%	0%	0%	0%	0%	7%	13%	0%
	#4	26%	53%	0%	38%	49%	0%	33%	46%	0%

For nKOM, the results show that only scenario #3 in O-mode is compatible with the global distribution, with $C_{max} = 39\%$. Scenario #2 in O-mode and scenarios #2, #3, and #4 in X-mode are compatible with the XO distribution, with $C_{max} = 51\%$, 50%, 47%, and 53%, respectively. Only scenario #3 in O-mode is compatible with the ZO distribution, with $C_{max} = 37\%$.

For nLF, the results show that scenarios #3 and #4 in O-mode and scenario #4 in X-mode are compatible with the global distribution, with $C_{max} = 41\%$, 41%, and 38%, respectively. Similarly, scenarios #3 and #4 in O-mode and scenario #4 in X-mode

are compatible with the XO distribution, with $C_{max} = 48\%$, 45% , and 49% , respectively. However, only scenario #4 in O-mode is compatible with the ZO distribution, with $C_{max} = 55\%$.

For nKOM+nLF, the results show that scenarios #3 and #4 in O-mode are compatible with the global distribution, with $C_{max} = 44\%$ and 45% , respectively. As for nLF, scenarios #3 and #4 in O-mode and scenario #4 in X-mode are compatible with the XO distribution, with $C_{max} = 46\%$, 41% , and 46% , respectively. However, the simulated distributions correlate better with nLF alone ($C_{max} = 48\%$, 45% , and 49%). As for nLF, only scenario #4 in O-mode is compatible with the ZO distribution, with $C_{max} = 54\%$. The simulated distribution is nearly as well correlated with nLF alone ($C_{max} = 55\%$).

Thus, we can summarize that:

- Scenario #1 is incompatible with nKOM and nLF observations. This incompatibility appears to be caused by the directivity predicted by Jones (1980).
- Scenario #2 is only compatible with nKOM observations in XO mode. This is expected since (i) ZO observations imply $\omega < \omega_{uh}$ and (ii) nLF observations in XO-mode are mainly distributed at frequencies too low to correspond to $2\omega_{uh}$.
- Scenarios #3 and #4 are both compatible with nKOM and nLF observations. nKOM in ZO is consistent with emissions generated at ω_{pe} for oblique α ($\sim 56^\circ$) and high ϵ ($\sim 80\%$). nLF in XO is compatible with emissions generated in O-mode at ω_{pe} and $2\omega_{pe}$ and in X-mode at $2\omega_{pe}$ for near-perpendicular α ($> 75^\circ$) and intermediate or low ϵ ($< 70^\circ$). nLF in ZO is consistent with emissions generated in O-mode at $2\omega_{pe}$ for near-parallel α ($< 15^\circ$) and very high ϵ ($> 90\%$).
- It is difficult to constrain the characteristics of nKOM in XO since it is compatible with scenarios #2, #3, and #4. However, they seem to converge toward (i) emissions in X-mode and (ii) values of $\alpha > 30^\circ$. Finally, even though none of these scenarios can be excluded, scenario #4 stands out: it has the highest correlation ($C_{max} = 53\%$ vs. $C_{max} \sim 50\%$) and is highly localized in the parameter space with $\alpha > 45^\circ$ and $\epsilon \sim 80\%$.

5 Comparison with the Juno/Waves Observations at PJ01

In the absence of polarization measurements, the Waves instrument does not allow for goniopolarimetry measurements of nKOM and nLF observations. However, due to Juno's high-latitude observation geometry, it was possible to perform goniometry measurements of nKOM and nLF on the day following the first perijove of Jupiter (PJ01) on 28/08/2016, using the spacecraft's rotation (Imai et al., 2017).

5.1 Radio Sources Location

Figures 4 and 5 show the distributions of nKOM and nLF radio sources in the plasma disk and the Io Plasma Torus (IPT), as measured by Juno/Waves during PJ01 and as predicted by LsPRESSO. In the following, we compare in details the predicted radio source locations for nKOM and nLF with those inferred from Juno/Waves observations during PJ01.

Panels (a) and (b) of Figure 4 show the meridian and equatorial projections, respectively, in the joventric reference frame of the nKOM radio sources predicted by LsPRESSO. The meridian distributions of nKOM radio sources predicted with LsPRESSO partially match the Juno/Waves observations. Scenarios #2, #3, and #4 (Figure 4.a2, a3, and a4) predict nKOM radio sources between $\sim 8 R_J$ and $\sim 9.5 R_J$. However, only scenarios #3 and #4 predict nKOM radio sources near the centrifugal equator at $> 11.5 R_J$. On the other hand, the equatorial distributions of nKOM radio sources predicted with

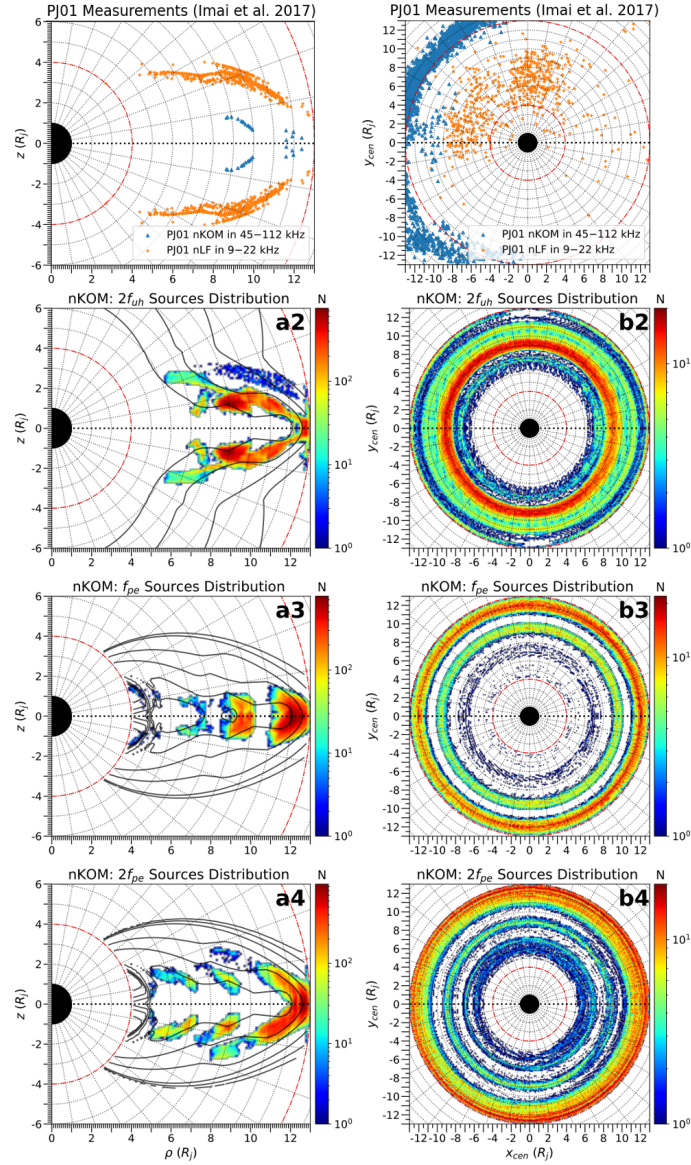


Figure 4. Meridian distributions (a2, a3, a4) and equatorial distributions (b2, b3, b4) of nKOM radio sources in the plasma disk and the Io Plasma Torus (IPT). Panels indexed 2, 3, and 4 correspond to sources predicted with LsPRESSO for the generation scenarios of the same number. Blue triangles and orange crosses indicate the positions of nKOM and nLF radio sources, respectively, as measured by Juno/Waves on 28/08/2016 and reconstructed from Figures 1a and 3 of Imai et al. (2017). The x-axes and y-axes represent respectively, for the left and right panels, the cylindrical coordinate ρ and z of the meridian plane and the cartesian coordinates x_{cen} and y_{cen} of the equatorial plane, both in the centrifugal referential. Jupiter's disk is displayed in black, the dotted circles around it mark radial distance by $1 R_J$ steps. The dotted lines mark respectively, for the left and right panels, latitudes and CML by 10° steps, with the bold dotted line indicating the centrifugal equator and the CML at 200.769° . The red dotted-dashed circles mark Imai's (2016) diffusive density model limits at $4 R_J$ and $13 R_J$. The meridian distribution on the top panel is mirrored around the centrifugal equator as they estimated the location of the radio sources originating from the southern hemisphere. The color scale is adjusted in each panel and represents the number of sources N . The color maps have 130×120 pixels. In panels (a2, a3, a4), the black contours correspond to the radio source frequencies $f = [5, 10, 20, 40, 80, 160]$ kHz (except for sources at $2\omega_{uh}$, where the first contour is at $f = 20$ kHz).

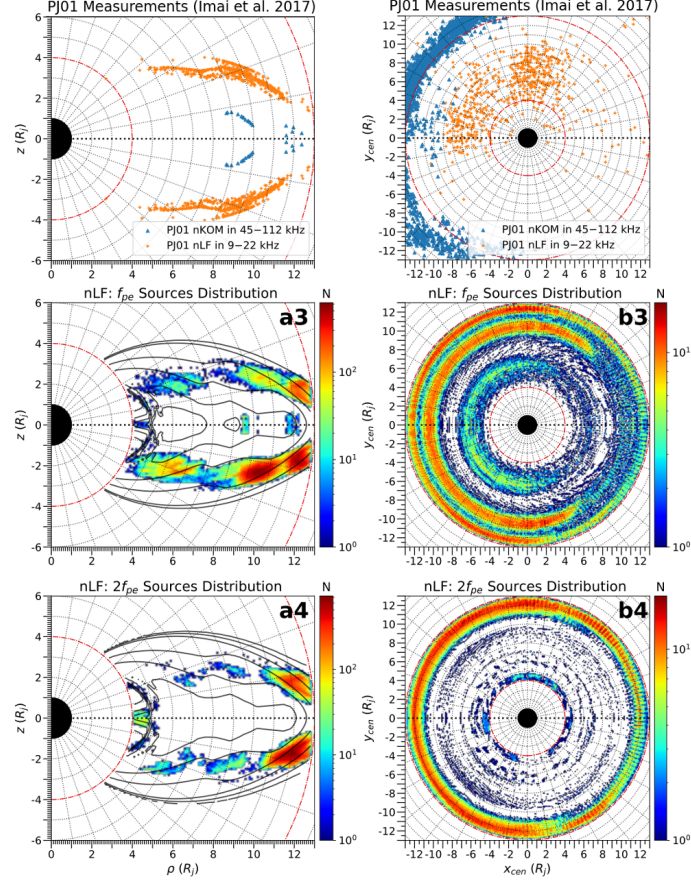


Figure 5. Meridian distributions (a3, a4) and equatorial distributions (b3, b4) of nLF radio sources in the plasma disk and the Io Plasma Torus (IPT), as measured by Juno/Waves and predicted with LsPRESSO for the compatible generation scenarios determined from Table 2. Panels indexed 3 and 4 correspond to sources predicted with LsPRESSO for the generation scenarios of the same number. The panel definitions are identical to those in Figure 4.

LsPRESSO do not match the Juno/Waves observations. Indeed, scenarios #2, #3, and #4 (Figure 4.b2, b3, and b4) predict an azimuthal symmetry around Jupiter’s centrifugal axis in the distribution of nKOM radio sources, whereas the observed sources are located at $x_{cen} < 0$.

Panels (a) and (b) of Figure 5 show the meridian and equatorial projections, respectively, in the joventric reference frame of the nLF radio sources predicted by LsPRESSO. The meridian distributions of nLF radio sources predicted with LsPRESSO match the Juno/Waves observations. Scenarios #3 and #4 (Figure 5.a3 and a4) predict nLF radio sources at $> 8.5 R_J$ on the edges of the plasma disk at latitudes of $\sim \pm 5^\circ$. Although the equatorial distributions of nLF radio sources predicted with LsPRESSO only partially match the Juno/Waves observations, scenario #3 (Figure 4.b3) predicts the azimuthal asymmetry around Jupiter’s centrifugal axis. Finally, it is also noticeable that scenario #3 appears to predict both the meridian and equatorial distributions of nKOM radio sources between $\sim 11.5 R_J$ and $\sim 12 R_J$.

Thus, the localization of nKOM and nLF radio sources observed by Juno/Waves is partially consistent with the predictions of LsPRESSO. The LsPRESSO predictions for nLF appear to explain the localization of both nKOM and nLF radio sources. These sources correspond to Jovian plasma emissions generated at the fundamental frequency ω_{pe} for an O-mode cutoff, with radio sources where $\nabla n_e \perp \mathbf{B}$. This generation scenario is the only one capable of reproducing the asymmetry in the longitudinal distribution of nKOM and nLF radio sources.

5.2 Time-Frequency Morphology

The time-frequency visibility maps simulated with LsPRESSO for each generation scenario can be directly compared with the Juno/Waves spectrograms. Figures 6 and 7 display the Juno/Waves observations on 28/08/2016, the day following PJ01, along with the visibility maps simulated for the generation scenarios that are compatible with the Juno/Waves observations of nKOM and nLF, respectively. In the following paragraphs, the visibility maps predicted by LsPRESSO are compared to the observations made by Juno/Waves for both nKOM and nLF.

The spectrogram of nKOM observations (2nd panel of Figure 6) shows that two events were catalogued as nKOM at 10h00 and 19h00, occurring between 45–115 kHz. The visibility maps for the generation scenarios compatible with the nKOM observations only partially predict the visibility of nKOM observed during PJ01. Scenarios #2, #3, and #4 (3rd, 4th, and 5th panels of Figure 6) exhibit similar morphologies, with scenario #4 appearing to best match the time period and frequency range of the nKOM observations. However, none of the simulated visibility maps reproduce the periodicity of nKOM observations, particularly the extinction between 13h00 and 18h00. Finally, it can be noted that in the low-frequency limit, scenario #3 with an X-mode cutoff appears to follow the high-frequency boundary of the nLF observations (cf Section 6).

The spectrogram of nLF observations (2nd panel of Figure 7) shows that two events were catalogued as nLF at 9h00 and 19h00, occurring between 10–25 kHz. The visibility maps for the generation scenarios compatible with the nLF observations correctly predict the visibility of nLF observed during PJ01. Scenarios #3 and #4 (3rd and 4th panels of Figure 7) exhibit similar morphologies. Scenario #4 with an X-mode cutoff appears to best match the frequency range of the nLF observation at 9h00. However, scenarios #3 and #4 seem to accurately represent the nLF observation at 19h00: the low-frequency part coincides with scenario #3, while the high-frequency part aligns well with scenario #4. Moreover, unlike the visibility maps simulated for the nKOM observations, those simulated for the nLF observations correctly represent the periodicity of nLF observations. Finally, scenario #4 with an O-mode cutoff also appears to correspond to a signal between 4h30 and 6h00 that was not catalogued.

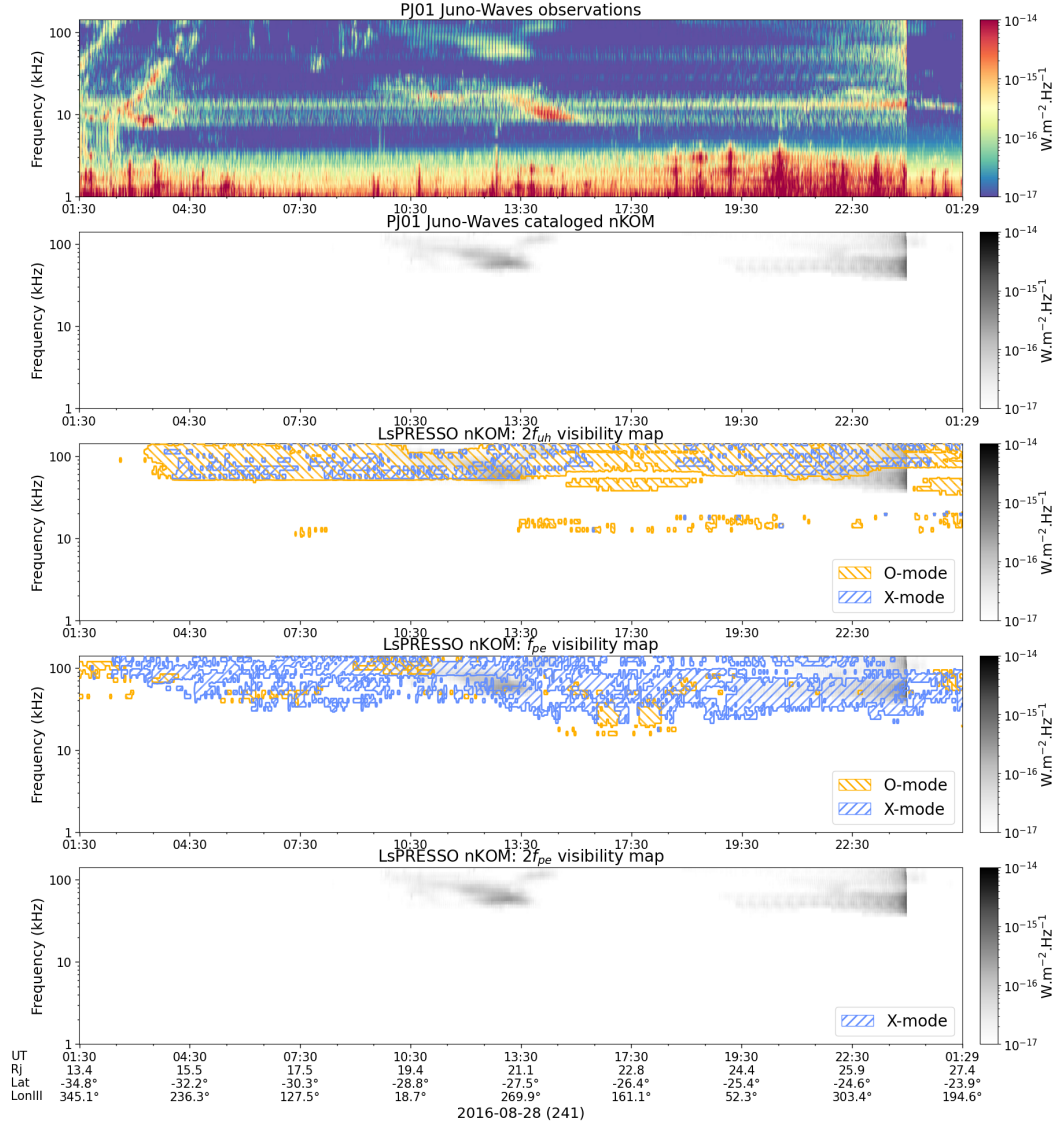


Figure 6. Comparison between nKOM observations by Juno/Waves during PJ01 and the visibility maps predicted by LsPRESSO for the compatible generation scenarios determined from Table 2. The first panel corresponds to the time-frequency spectrogram of the calibrated Juno/Waves observations. The second panel shows the time-frequency spectrogram of the calibrated nKOM observations by Juno/Waves. The intensity gap between the observations of 28/08/2016 (right after 00:00) and 29/08/2016 are due to the calibration process. The third, fourth, and fifth panels display the nKOM observations by Juno/Waves, overlaid with the time-frequency visibility maps of nKOM predicted by LsPRESSO for generation scenarios #2, #3, and #4, respectively (see Table 2). The orange and blue hatched regions correspond to the intercepted beams for O-mode and X-mode cutoffs, respectively. For all panels, the x-axes represent the observation period (UT), radial distance (R_J), jovian latitude (Lat), and System III longitude (LonIII) of Juno. The y-axes correspond to the Juno/Waves observation frequencies between channels #16 and #60 (i.e., from 1 kHz to 141 kHz) on a logarithmic scale.

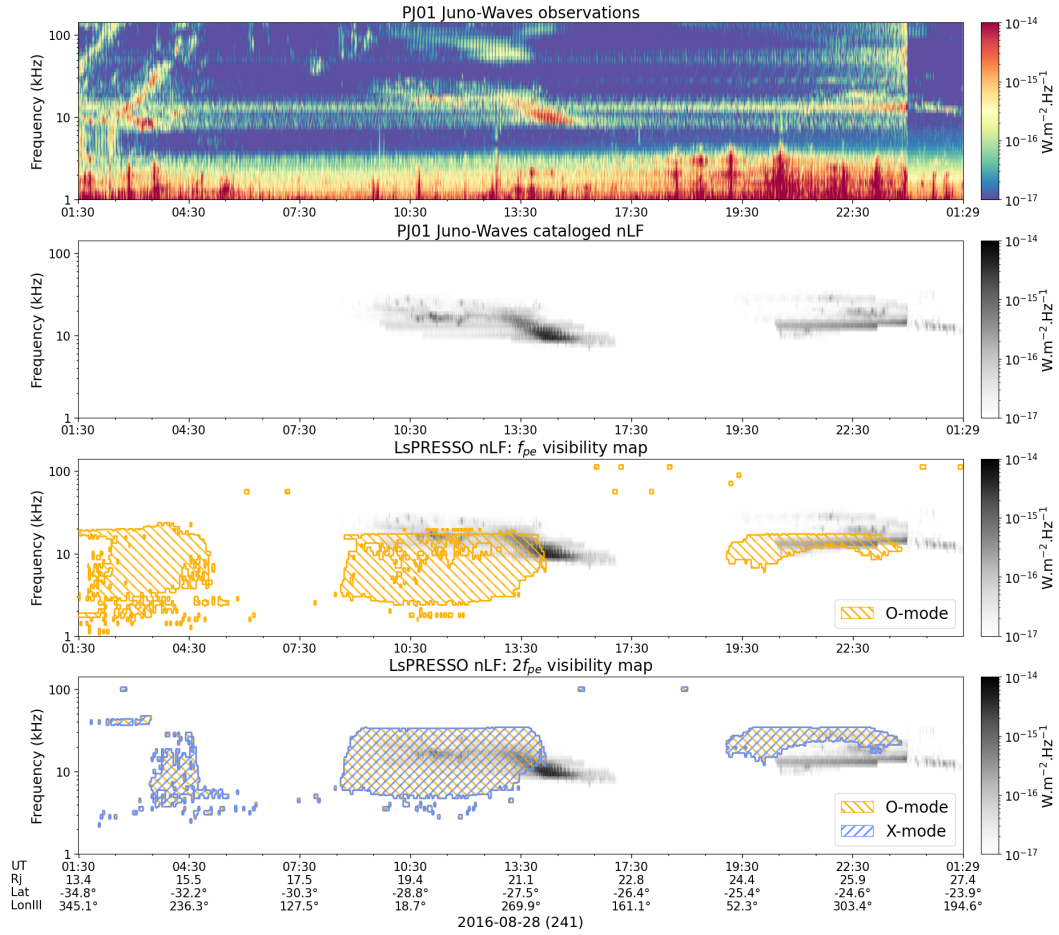


Figure 7. Comparison between nLF observations by Juno/Waves during PJ01 and the visibility maps predicted by LsPRESSO for the compatible generation scenarios determined from Table 2. The panel definitions are identical to those in Figure 6.

6 Conclusion and Discussion

We developed the LsPRESSO code, which simulates the visibility of planetary plasma emissions, and used it to study the generation and localization of nKOM and nLF radio sources based on the statistical analysis of Juno/Waves observations. Using the diffusive density model of Imai et al. (2017) and the VIP4 magnetic field model with current sheet (Connerney et al., 1998), we simulated the observation of Jovian plasma emissions by Juno/Waves exploring four different generation scenarios (see Table 1). Assuming that the activation of radio sources is controlled by the angle α between ∇n_e and \mathbf{B} , as well as the large-scale density gradient magnitude $\|\nabla n_e\|$ (characterized by its percentile ϵ), we compared the latitude-frequency distributions derived from the simulated visibility maps with those observed by Juno/Waves. This allowed us to determine which generation scenarios are capable of reproducing the observations.

Scenario #1, based on the theory of Jones (1987), is incompatible with the Juno/Waves observations of nKOM and nLF. Indeed, the predicted apparent emission directivity following the angle $\beta = \arctan(\sqrt{\omega_{pe}/\omega_{ce}})$ relative to \mathbf{B} does not explain the latitudinal distribution of Juno/Waves observations.

Scenario #3 in O-mode, which corresponds to emissions generated at ω_{pe} in the direction $\mathbf{r} \parallel -\nabla n_e$, is compatible with both nKOM and nLF observations by Juno/Waves. This scenario can separately reproduce nKOM observations in ZO (when $\alpha \sim 57^\circ$ and $\epsilon \sim 80\%$) and nLF observations in XO (when $\alpha \sim 90^\circ$ and $\epsilon < 70\%$). Moreover, it is noticeable that the simulated distribution for nLF in XO (see Figure S9.b3 in the Supplementary Information) also presents occurrences at high-latitudes similar to nKOM observations in ZO. Simulations by Schleyer et al. (2013); Kim et al. (2013) have shown that LMC of Langmuir waves to O-mode is efficient for large angles ($\angle(\nabla n_e, \mathbf{B}) > 70^\circ$), but also for intermediate angles ($40^\circ < \angle(\nabla n_e, \mathbf{B}) < 60^\circ$) when the plasma is moderately magnetized. This suggests that nKOM in ZO and part of nLF in XO are generated at ω_{pe} in O-mode via LMC mechanisms. Furthermore, the LMC theory of Jones (1980) predicts efficient conversions when $\nabla n_e \perp \mathbf{B}$, suggesting that near the O-mode cutoff, beam alignment tends to follow the anti-parallel density gradient direction rather than the angle β .

Scenario #4, which corresponds to emissions generated at $2\omega_{pe}$ in the anti-parallel density gradient direction, is compatible with the Juno/Waves observations of nLF. This scenario can reproduce nLF observations in ZO in O-mode (when $\alpha < 15^\circ$ and $\epsilon > 90\%$) and nLF observations in XO in both O-mode and X-mode (when $\alpha > 75^\circ$ and $\epsilon > 70\%$). This suggests that nLF in ZO and part of nLF in XO are generated at $2\omega_{pe}$ through NLMC mechanisms. Since emissions at $2\omega_{pe}$ can occur far from the O-mode and X-mode cutoffs, it is difficult to explain without ray-tracing models why the beam directivity is $\mathbf{r} \parallel -\nabla n_e$. However, as these emissions are generated when $\nabla n_e \parallel |\mathbf{B}|$ (for nLF in ZO) and $\nabla n_e \perp |\mathbf{B}|$ (for nLF in XO), their directivities may correspond to $\mathbf{r} \parallel |\mathbf{B}|$ and $\mathbf{r} \perp |\mathbf{B}|$, respectively.

Scenario #2, based on the theory of Fung and Papadopoulos (1987), along with scenarios #3 and #4, are compatible with some of the Juno/Waves observations of nKOM. Scenario #2 in both O-mode and X-mode, and scenarios #3 and #4 in X-mode, can reproduce nKOM observations in XO (when $\alpha > 30^\circ$). The simulated distributions in X-mode for scenarios #3 and #4 (see Figures S4.b3 and b4 in the Supplementary Information) are qualitatively more similar than those simulated under scenario #2 (see Figures S3.b2 and S4.b2 in the Supplementary Information). They are also able to reproduce the absence of occurrences around ~ 100 kHz. However, the results remain quantitatively ambiguous and do not allow for a conclusive determination of the generation and directivity of nKOM in XO.

Finally, for the generation scenarios compatible with the Juno/Waves observations of nKOM and nLF, the radio sources and time-frequency visibility maps predicted by LsPRESSO were compared with goniometry measurements and spectrograms obtained at PJ01 by Imai et al. (2017). For nKOM, the equatorial distribution of radio sources does not predict the azimuthal asymmetry observed by Juno/Waves, and the visibility maps do not reproduce the ~ 10.5 -hour periodicity. However, both of these properties are correctly reproduced in the case of nLF.

This difference may be explained by the intermittency of nKOM. Observations by Galileo have shown that the activation of nKOM radio sources is constrained by energetic events in Jupiter’s magnetosphere (Louarn et al., 1998, 2000, 2001). However, in this study, we assumed that plasma radio source activation is permanent. This implies that in the simulated visibility maps, only a fraction of the considered sources were actually active. Finally, although the comparison between LsPRESSO simulations and Imai et al. (2017) estimations gives new insights on the radio sources locations, the assumptions on the goniometry method have limitations, especially for the meridian case, as they assumed generation at ω_{pe} and deduced the projection employing the same time-averaged diffusive density model as the one used in this study (Imai, 2016).

On the other hand, since this issue is not observed with nLF, it suggests that the radio sources detected during the southern plasma disk crossing are more persistent. This implies that nLF could be less intermittent than nKOM, and its generation may not be primarily controlled by magnetospheric disturbances.

These nLF observations correspond to plasma emissions generated at ω_{pe} and $2\omega_{pe}$. They originate from the same radio sources at $> 10 R_J$ where $\nabla n_e \perp \mathbf{B}$, indicating the coexistence of LMC and NLMC mechanisms. In Louis et al. (2021b), the latitude-frequency distribution of nLF intensity suggests that nLF events are more intense at mid-latitudes when < 15 kHz (see Figure 4.b of Louis et al., 2021b). The predicted visibility maps for PJ01 (see Figure 7) also show that at 16h00, the observed event matching ω_{pe} is more intense than the one matching $2\omega_{pe}$. This could suggest that the linear conversion process dominates over nonlinear processes, indicating that the radio sources exhibit density fluctuations similar to those simulated by Krafft and Savoini (2021); Krafft and Volokitin (2024); Krafft et al. (2024).

Appendix A Propagation Mode Identification using the JADE and MAG instruments

Assuming a cold collisionless magnetized plasma, we can derive the frequency ranges of the normal modes of the plasma as a function of ω_{pe} and ω_{ce} using the *Altar-Appleton-Hartree* relation (Appleton, 1932):

$$\epsilon(\omega) = 1 - \frac{2X(1 - X)}{2(1 - X) - Y^2 \sin^2 \theta \pm \sqrt{(Y^2 \sin^2 \theta)^2 + 4Y^2(1 - X^2) \cos^2 \theta}} \quad (\text{A1})$$

with $X = \omega_{pe}^2/\omega^2$ and $Y = \omega_{ce}/\omega$.

Figure A1 illustrates this for two different ratio of ω_{pe} over ω_{ce} : (a) for $\omega_{pe}/\omega_{ce} = 2$, (b) $\omega_{pe}/\omega_{ce} = 1/2$. Figure A2 shows the 24-hour spectrograms of the calibrated nKOM and nLF observations (a) on the day before (28/08/2018) and (b) on the day after (30/08/2018) PJ16, overlaid with the frequency ranges in ZW, XO, and ZO (see their definitions Section 3.2). Panel (a) indicates that during the northern crossing of the plasma disk, all nKOM events are observed in XO. Panel (b) shows that during the southern crossing of the plasma disk, the nLF event at 03h00 is observed in ZO, whereas all nKOM and nLF events after 06h00 are observed in XO. However, the nLF events at 03h00 and 06h00 appear to be connected and were individually contoured due to the presence of QP at

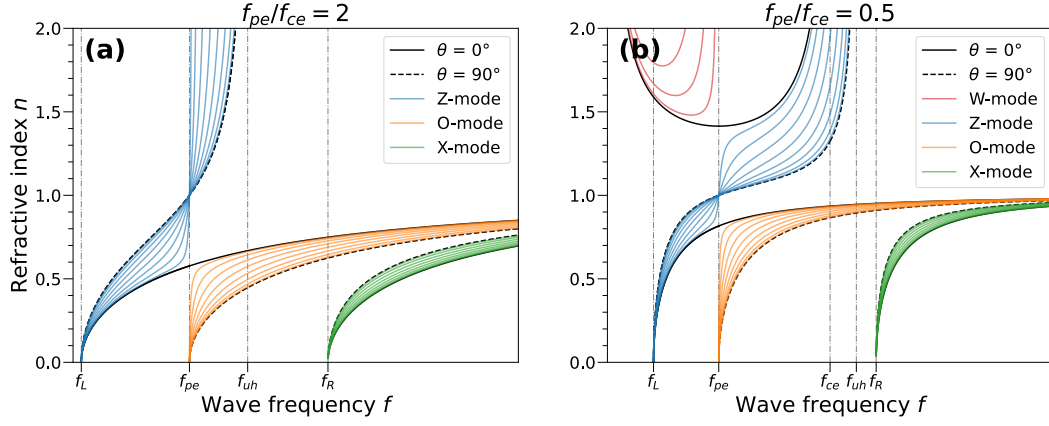


Figure A1. Dispersion curves of a cold, homogeneous, collisionless plasma immersed in a uniform magnetic field. Panels (a) and (b) correspond to the solutions of the dispersion relation defined by Equation (A1) for different values of θ when $\omega_{pe}/\omega_{ce} = 2$ and $\omega_{pe}/\omega_{ce} = 1/2$ with $\omega = 2\pi f$. The red, blue, orange, and green curves correspond to the W, Z, O, and X modes, respectively, for $\theta \in]0^\circ, 90^\circ[$. The solid and dashed black curves correspond to $\theta = 0^\circ$ and $\theta = 90^\circ$, respectively.

05h00 (see Figure 1). In this case, as the nLF event is at the intersection between ZO and XO, this suggests that it propagates in O-mode.

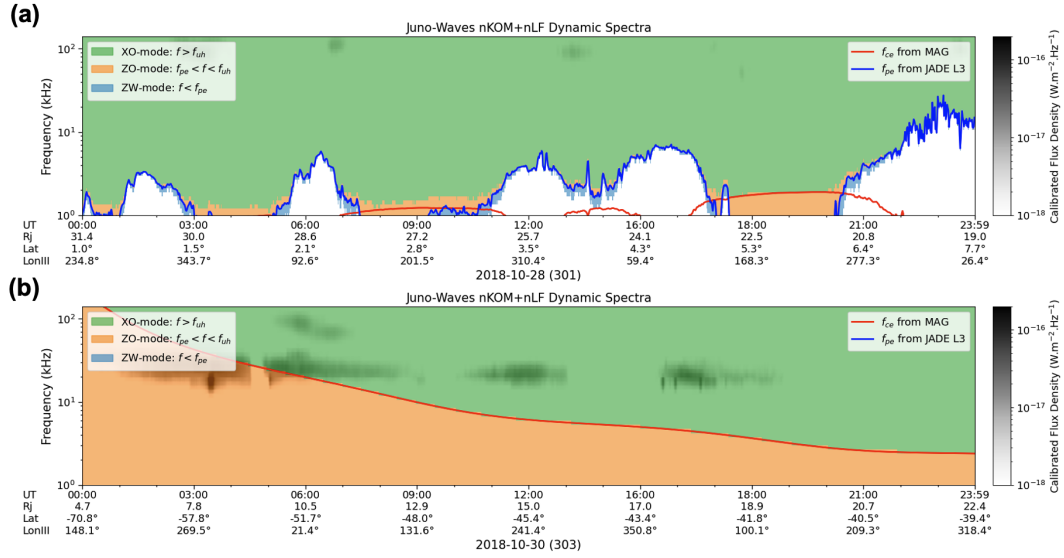


Figure A2. 24-hour spectrograms of the calibrated nKOM and nLF observations by Waves compared to the ZW, XO, and ZO spectral ranges in the plasma disk (a) on the day before (28/10/2018) and (b) on the day after (30/10/2018) PJ16. The x- and y-axes are identical to those in Figure 1. The blue, orange, and green areas correspond to the ZW, ZO, and XO frequency ranges, respectively, estimated from JADE and MAG data. The red curve represents the electron cyclotron frequency $f_{ce} = \omega_{ce}/2\pi$ derived from MAG data. The blue curve represents the plasma frequency $f_{pe} = \omega_{pe}/2\pi$ derived from JADE data.

Data Availability Statement

The Juno/Waves calibrated data used in the manuscript is available at <https://doi.org/10.25935/6jg4-mk86> (Louis et al., 2021c). The Juno/Waves catalog used in the manuscript is available at <https://doi.org/10.25935/nhb2-wy29> (Louis et al., 2021a).

Acknowledgments

A. Boudouma's work at LIRA was supported by the CNES (Centre National d'Etudes Spatiale). A. Boudouma's work at the Department of Space Physics of the Institute of Atmospheric Physics is supported by the Lumina Quaeruntur fellowship (LQ100422501) of the Czech Academy of Sciences.

References

- Appleton, E. V. (1932). Wireless studies of the ionosphere. *Institution of Electrical Engineers-Proceedings of the Wireless Section of the Institution*, 7(21), 257–265.
- Ashour-Abdalla, M., & Okuda, H. (1984). Generation of ordinary mode electromagnetic radiation near the upper hybrid frequency in the magnetosphere. *Journal of Geophysical Research: Space Physics*, 89(A10), 9125–9131. Retrieved from <https://agupubs.onlinelibrary.wiley.com/doi/abs/10.1029/JA089iA10p09125> doi: <https://doi.org/10.1029/JA089iA10p09125>
- Bacchini, F., & Philippov, A. A. (2024, March). Fundamental, harmonic, and third-harmonic plasma emission from beam-plasma instabilities: a first-principles precursor for astrophysical radio bursts. *MNRAS*, 529(1), 169–177. doi: 10.1093/mnras/stae521
- Barbosa, D. D. (1982, May). Low-level VLF and LR radio emissions observed at earth and Jupiter. *Reviews of Geophysics and Space Physics*, 20, 316–334. doi: 10.1029/RG020i002p00316
- Boardsen, S. A., Kim, E.-H., Green, J. L., Cheng, C. Z., Cairns, I. H., & Johnson, J. R. (2023). Statistical study of the nonthermal continuum radiation beaming angle measured by the high frequency receiver on van allen probe-a. *Journal of Geophysical Research: Space Physics*, 128(9), e2023JA031426. Retrieved from <https://agupubs.onlinelibrary.wiley.com/doi/abs/10.1029/2023JA031426> (e2023JA031426 2023JA031426) doi: <https://doi.org/10.1029/2023JA031426>
- Boudouma, A., Zarka, P., Louis, C. K., Briand, C., & Imai, M. (2024). Generation mechanism and beaming of jovian nkom from 3d numerical modeling of juno/waves observations. *J. Geophys. Res.*, 129(4), e2023JA032280. (B24) doi: <https://doi.org/10.1029/2023JA032280>
- Briand, C., Henri, P., & Hoang, S. (2014, April). Inhibition of type III radio emissions due to the interaction between two electron beams: Observations and simulations. *J. Geophys. Res.*, 119(4), 2365–2378. doi: 10.1002/2013JA019688
- Budden, K. G., & Jones, D. (1987, January). The Theory of Radio Windows in Planetary Magnetospheres. *Proceedings of the Royal Society of London Series A*, 412(1842), 1–23. doi: 10.1098/rspa.1987.0077
- Cairns, I. H., & Willes, A. J. (2005, May). Angle-averaged efficiencies for linear mode conversion between Langmuir waves and radiation in an unmagnetized plasma. *Physics of Plasmas*, 12(5), 052315. doi: 10.1063/1.1889123
- Carr, T. D., Desch, M. D., & Alexander, J. K. (1983). Physics of the Jovian magnetosphere. 7. Phenomenology of magnetospheric radio emissions. In *Physics of the jovian magnetosphere* (p. 226–284).
- Connerney, J. E. P., Acuña, M. H., Ness, N. F., & Satoh, T. (1998). New models of jupiter's magnetic field constrained by the io flux tube footprint. *J. Geophys. Res.*, 103(A6), 11929–11939. doi: <https://doi.org/10.1029/97JA03726>

- Connerney, J. E. P., Benn, M., Bjarno, J. B., Denver, T., Espley, J., Jorgensen, J. L., ... Smith, E. J. (2017, November). The Juno Magnetic Field Investigation. *Space Sci. Rev.*, *213*(1-4), 39-138. doi: 10.1007/s11214-017-0334-z
- Daigne, G., & Leblanc, Y. (1986, July). Narrow-band Jovian kilometric radiation: occurrence, polarization, and rotation period. *Journal of Geophysical Research*, *91*(A7), 7961-7969. doi: 10.1029/JA091iA07p07961
- Fung, S. F., & Papadopoulos, K. (1987, August). The emission of narrow-band Jovian kilometric radiation. *Journal of Geophysical Research*, *92*(A8), 8579-8593. doi: 10.1029/JA092iA08p08579
- Gurnett, D. A., Kurth, W. S., & Scarf, F. L. (1983, March). Narrowband electromagnetic emissions from Jupiter's magnetosphere. *Nature*, *302*(5907), 385-388. doi: 10.1038/302385a0
- Henri, P., Califano, F., Briand, C., & Mangeney, A. (2010). Vlasov-poisson simulations of electrostatic parametric instability for localized langmuir wave packets in the solar wind. *J. Geophys. Res.*, *115*(A6). Retrieved from <https://agupubs.onlinelibrary.wiley.com/doi/abs/10.1029/2009JA014969> doi: <https://doi.org/10.1029/2009JA014969>
- Henri, P., Sgattoni, A., Briand, C., Amiranoff, F., & Riconda, C. (2019, March). Electromagnetic Simulations of Solar Radio Emissions. *Journal of Geophysical Research (Space Physics)*, *124*(3), 1475-1490. doi: 10.1029/2018JA025707
- Imai, M. (2016). *Characteristics of jovian low-frequency radio emissions during the cassini and voyager flyby of jupiter* (Doctoral dissertation, Kyoto University, Kyoto, Japan). doi: 10.14989/doctor.k19504
- Imai, M., Kurth, W. S., Hospodarsky, G. B., Bolton, S. J., Connerney, J. E. P., & Levin, S. M. (2017). Direction-finding measurements of jovian low-frequency radio components by juno near perijove 1. *Geophysical Research Letters*, *44*(13), 6508-6516. Retrieved from <https://agupubs.onlinelibrary.wiley.com/doi/abs/10.1002/2017GL072850> doi: <https://doi.org/10.1002/2017GL072850>
- Jones, D. (1980, November). Latitudinal beaming of planetary radio emissions. *Nature*, *288*(5788), 225-229. doi: 10.1038/288225a0
- Jones, D. (1987, June). Io plasma torus and the source of jovian narrow-band kilometric radiation. *Nature*, *327*(6122), 492-495. doi: 10.1038/327492a0
- Kaiser, M. L., & Desch, M. D. (1980). Narrow-band jovian kilometric radiation: A new radio component. *Geophysical Research Letters*, *7*(5), 389-392. doi: <https://doi.org/10.1029/GL007i005p00389>
- Kaiser, M. L., & Desch, M. D. (1980, May). Narrow-band Jovian kilometric radiation: A new radio component. *Geophys. Res. Lett.*, *7*(5), 389-392. doi: 10.1029/GL007i005p00389
- Kaiser, M. L., Desch, M. D., Farrell, W. M., MacDowall, R. J., Stone, R. G., Lecacheux, A., ... Zarka, P. (1992). Ulysses observations of escaping vlf emissions from jupiter. *Geophysical Research Letters*, *19*(7), 649-652. Retrieved from <https://agupubs.onlinelibrary.wiley.com/doi/abs/10.1029/92GL00387> doi: <https://doi.org/10.1029/92GL00387>
- Kim, E.-H., Cairns, I. H., & Johnson, J. R. (2013, December). Linear mode conversion of Langmuir/z-mode waves to radiation in plasmas with various magnetic field strength. *Physics of Plasmas*, *20*(12), 122103. doi: 10.1063/1.4837515
- Kim, E.-H., Cairns, I. H., & Robinson, P. A. (2007, July). Extraordinary-Mode Radiation Produced by Linear-Mode Conversion of Langmuir Waves. *Phys. Rev. Lett.*, *99*(1), 015003. doi: 10.1103/PhysRevLett.99.015003
- Kim, E.-H., Cairns, I. H., & Robinson, P. A. (2008, October). Mode conversion of Langmuir to electromagnetic waves at magnetic field-aligned density inhomogeneities: Simulations, theory, and applications to the solar wind and the corona. *Physics of Plasmas*, *15*(10), 102110-102110. doi: 10.1063/1.2994719
- Krafft, C., & Savoini, P. (2021, August). Second Harmonic Electromagnetic Emis-

- sions by an Electron Beam in Solar Wind Plasmas with Density Fluctuations. *ApJ*, *917*(2), L23. doi: 10.3847/2041-8213/ac1795
- Krafft, C., Savoini, P., & Polanco-Rodríguez, F. J. (2024, June). Mechanisms of Fundamental Electromagnetic Wave Radiation in the Solar Wind. *ApJ*, *967*(2), L20. doi: 10.3847/2041-8213/ad47b5
- Krafft, C., & Volokitin, A. S. (2024, March). Second Harmonic Electromagnetic Wave Emissions from a Turbulent Plasma with Random Density Fluctuations. *ApJ*, *964*(1), 65. doi: 10.3847/1538-4357/ad20ee
- Louarn, P., Mauk, B. H., Kivelson, M. G., Kurth, W. S., Roux, A., Zimmer, C., ... Williams, D. J. (2001, December). A multi-instrument study of a Jovian magnetospheric disturbance. *J. Geophys. Res.*, *106*(A12), 29883-29898. doi: 10.1029/2001JA900067
- Louarn, P., Paranicas, C. P., & Kurth, W. S. (2014, June). Global magnetodisk disturbances and energetic particle injections at Jupiter. *J. Geophys. Res.*, *119*(6), 4495-4511. doi: 10.1002/2014JA019846
- Louarn, P., Roux, A., Perraut, S., Kurth, W., & Gurnett, D. (1998, January). A study of the large-scale dynamics of the Jovian magnetosphere using the Galileo Plasma Wave Experiment. *Geophys. Res. Lett.*, *25*(15), 2905-2908. doi: 10.1029/98GL01774
- Louarn, P., Roux, A., Perraut, S., Kurth, W. S., & Gurnett, D. A. (2000, June). A study of the Jovian “energetic magnetospheric events” observed by Galileo: role in the radial plasma transport. *J. Geophys. Res.*, *105*(A6), 13073-13088. doi: 10.1029/1999JA900478
- Louis, C. K., Zarka, P., & Cecconi, B. (2021c). *Juno/Waves estimated flux density Collection (Version 1.0)*. PADC/MASER. doi: 10.25935/6jg4-mk86
- Louis, C. K., Zarka, P., Cecconi, B., & Kurth, W. S. (2021a). *Catalogue of Jupiter radio emissions identified in the Juno/Waves observations (Version 1.0)*. PADC/MASER. doi: 10.25935/nhb2-wy29
- Louis, C. K., Zarka, P., Dabidin, K., Lampson, P. A., Magalhães, F. P., Boudouma, A., ... Cecconi, B. (2021b, October). Latitudinal Beaming of Jupiter’s Radio Emissions From Juno/Waves Flux Density Measurements. *Journal of Geophysical Research (Space Physics)*, *126*(10), e29435. doi: 10.1029/2021JA029435
- McComas, D. J., Alexander, N., Allegrini, F., Bagenal, F., Beebe, C., Clark, G., ... White, D. (2017, November). The Jovian Auroral Distributions Experiment (JADE) on the Juno Mission to Jupiter. *Space Sci. Rev.*, *213*(1-4), 547-643. doi: 10.1007/s11214-013-9990-9
- Melrose, D. B. (1981, January). A theory for the nonthermal radio continua in the terrestrial and jovian magnetospheres. *J. Geophys. Res.*, *86*(A1), 30-36. doi: 10.1029/JA086iA01p00030
- Menietti, J. D., Yoon, P. H., Averkamp, T. F., Kurth, W. S., Faden, J. B., Allegrini, F., ... Bolton, S. J. (2023, May). Wave and Particle Analysis of Z-Mode and O-Mode Emission in the Jovian Inner Magnetosphere. *Journal of Geophysical Research (Space Physics)*, *128*(5), e2022JA031199. doi: 10.1029/2022JA031199
- Perraut, S., Roux, A., Louarn, P., Gurnett, D. A., Kurth, W. S., & Khurana, K. K. (1998). Mode conversion at the jovian plasma sheet boundary. *Journal of Geophysical Research: Space Physics*, *103*(A7), 14995-15000. Retrieved from <https://agupubs.onlinelibrary.wiley.com/doi/abs/10.1029/97JA02879> doi: <https://doi.org/10.1029/97JA02879>
- Reiner, M. J., Fainberg, J., Stone, R. G., Kaiser, M. L., Desch, M. D., Manning, R., ... Pedersen, B. M. (1993, July). Source characteristics of Jovian narrow-band kilometric radio emissions. *Journal of Geophysical Research*, *98*(E7), 13163-15000. doi: 10.1029/93JE00536
- Ronmark, K. (1989, July). Myriametric radiation and the efficiency of linear mode conversion. *Geophys. Res. Lett.*, *16*(7), 731-734. doi: 10.1029/

- GL016i007p00731
- Schleyer, F., Cairns, I. H., & Kim, E. H. (2013, March). Linear mode conversion of Langmuir/z-mode waves to radiation: Scalings of conversion efficiencies and propagation angles with temperature and magnetic field orientation. *Physics of Plasmas*, *20*(3), 032101. doi: 10.1063/1.4793726
- Schleyer, F., Cairns, I. H., & Kim, E.-H. (2014). Linear mode conversion of langmuir/z mode waves to radiation: Averaged energy conversion efficiencies, polarization, and applications to earth's continuum radiation. *Journal of Geophysical Research: Space Physics*, *119*(5), 3392-3410. Retrieved from <https://agupubs.onlinelibrary.wiley.com/doi/abs/10.1002/2013JA019364> doi: <https://doi.org/10.1002/2013JA019364>
- Stone, R. G., Pedersen, B. M., Harvey, C. C., Canu, P., Cornilleau-Wehrin, N., Desch, M. D., ... Zarka, P. (1992, September). Ulysses Radio and Plasma Wave Observations in the Jupiter Environment. *Science*, *257*(5076), 1524-1531. doi: 10.1126/science.257.5076.1524
- Thurgood, J. O., & Tsiklauri, D. (2015, December). Self-consistent particle-in-cell simulations of fundamental and harmonic plasma radio emission mechanisms. *A&A*, *584*, A83. doi: 10.1051/0004-6361/201527079
- Treumann, R. A. (2006, August). The electron-cyclotron maser for astrophysical application. *The Astronomy and Astrophysics Review*, *13*(4), 229-315. doi: 10.1007/s00159-006-0001-y
- Warwick, J. W., Pearce, J. B., Peltzer, R. G., & Riddle, A. C. (1977, December). Planetary Radio Astronomy Experiment for Voyager Missions. *Space Sci. Rev.*, *21*(3), 309-327. doi: 10.1007/BF00211544
- Warwick, J. W., Pearce, J. B., Riddle, A. C., Alexander, J. K., Desch, M. D., Kaiser, M. L., ... Staelin, D. H. (1979a, November). Planetary Radio Astronomy Observations from Voyager 2 Near Jupiter. *Science*, *206*(4421), 991-995. doi: 10.1126/science.206.4421.991
- Warwick, J. W., Pearce, J. B., Riddle, A. C., Alexander, J. K., Desch, M. D., Kaiser, M. L., ... Pedersen, B. M. (1979b, June). Voyager 1 Planetary Radio Astronomy Observations Near Jupiter. *Science*, *204*(4396), 995-998. doi: 10.1126/science.204.4396.995
- Zarka, P., Cecconi, B., & Kurth, W. S. (2004, September). Jupiter's low-frequency radio spectrum from Cassini/Radio and Plasma Wave Science (RPWS) absolute flux density measurements. *Journal of Geophysical Research (Space Physics)*, *109*(A9), A09S15. doi: 10.1029/2003JA010260